



## RESEARCH LETTER

10.1029/2024GL110810

## What Are the Finger-Like Clouds in the Hurricane Inner-Core Region?

Kun Gao<sup>1,2</sup> , Joseph Mouallem<sup>1,2</sup> , and Lucas Harris<sup>3</sup> <sup>1</sup>Program in Atmospheric and Oceanic Sciences, Princeton University, Princeton, NJ, USA, <sup>2</sup>Cooperative Institute for Modeling the Earth System, Princeton University, Princeton, NJ, USA, <sup>3</sup>NOAA/Geophysical Fluid Dynamics Laboratory, Princeton, NJ, USA

## Key Points:

- We conduct a O(100 m) grid spacing simulation that captures the finger-like features along the inner edge of the hurricane eyewall
- We propose a mechanism that links the finger cloud formation and hurricane-scale dynamics
- This proposed mechanism explains the emergence time, frequency, radial location and vertical extent of the finger features

## Supporting Information:

Supporting Information may be found in the online version of this article.

## Correspondence to:

K. Gao,  
[kun.gao@noaa.gov](mailto:kun.gao@noaa.gov)

## Citation:

Gao, K., Mouallem, J., & Harris, L. (2024). What are the finger-like clouds in the Hurricane inner-core region? *Geophysical Research Letters*, 51, e2024GL110810. <https://doi.org/10.1029/2024GL110810>

Received 17 JUN 2024

Accepted 23 OCT 2024

## Author Contributions:

**Conceptualization:** Kun Gao  
**Formal analysis:** Kun Gao  
**Funding acquisition:** Lucas Harris  
**Methodology:** Kun Gao, Joseph Mouallem, Lucas Harris  
**Project administration:** Lucas Harris  
**Software:** Joseph Mouallem  
**Visualization:** Kun Gao  
**Writing – original draft:** Kun Gao  
**Writing – review & editing:** Kun Gao, Joseph Mouallem, Lucas Harris

**Abstract** Finger-like km-scale features have been observed along the inner-edge of the eyewall of intense hurricanes. But due to the limited availability of observations, many important aspects of these features remain unknown. In this study, we aim to offer insights on the nature of these phenomena based on a four-day-duration O(100 m) grid spacing simulation that covers the inner-core region of an idealized hurricane. The simulation successfully captured the finger-like features, which closely resemble observed ones. We propose that these features are formed due to the shear instability associated with vertical distribution of the tangential wind in the inner-core region. This proposed mechanism offers insights on several key characteristics of the features of interest, including their emergence time, frequency, radial location and vertical extent. Our study also demonstrates the feasibility of using multi-level nesting for O(100 m) grid spacing hurricane simulations and predictions, aligning with the goals for next generation hurricane models.

**Plain Language Summary** The inner core region of hurricanes harbors complex dynamical features, including small-scale clouds characterized by finger-like appearances pointing toward the hurricane eye. These features have been frequently observed in intense hurricanes. However, many basic aspects of these features remain unknown, particularly regarding what controls their occurrence and location. We conduct a numerical simulation with a very fine (about 100 m) horizontal grid spacing to investigate the nature of these features. Our proposed mechanism explains several key characteristics of these features.

## 1. Introduction

The inner region of Tropical Cyclones (TCs) harbors complex dynamical features, among which are the O(10 km) mesovortices that are possibly associated with vortex Rossby waves (e.g., Kossin & Schubert, 2004) and the finer O(1 km) periodic striation features that exist along the inner edge of the eyewall. Various observational studies have confirmed the existence of the striation features under intense TCs, which manifest themselves as high reflectivity filaments in the radar observations that are located at the inner edge of the eyewall, or significant wind gusts in the near surface wind fields (e.g., Aberson et al., 2006; Mashiko & Shimada, 2021; Tsukada & Horinouchi, 2020). The radar reflectivity caused by these features exhibits a distinctive appearance resembling fingers pointing toward the TC eye, and therefore we will refer to them as finger clouds hereafter. Similar features have also been captured by numerical simulations with O(100 m) or even finer scale grid spacing that cover the TC inner core region (e.g., Ito et al., 2017; Rotunno et al., 2009), although the direct relation between the simulated and the observed features has not been established. Despite the observational and numerical evidence, it remains unknown what causes these features, why they are oriented radially within the eyewall, and why they occur frequently in strong TCs.

In this study we present an analysis based on a O(100 m) grid spacing simulation that covers the entire core region of an idealized TC throughout its entire intensification period. The simulation successfully captured the finger clouds along the inner-edge of the eyewall, closely resembling the observed features. We aim to offer insight on the characteristics of these features based on our high-resolution model data, and propose a physical mechanism that links their formation to the TC-scale dynamics.

## 2. Methodology

## 2.1. Nested Domain Setup

The model we use is the Geophysical Fluid Dynamics Laboratory (GFDL) System for High-resolution prediction on Earth-to-Local Domains (SHiELD; Harris et al., 2020), which is built upon the nonhydrostatic Finite-Volume

© 2024. The Author(s).

This is an open access article under the terms of the [Creative Commons Attribution-NonCommercial-NoDerivs License](https://creativecommons.org/licenses/by/4.0/), which permits use and distribution in any medium, provided the original work is properly cited, the use is non-commercial and no modifications or adaptations are made.

Cubed-Sphere (FV3) dynamical core and allows for flexible multi-level nested configurations (Mouallem et al., 2022). In this study we conduct an idealized TC simulation, in which the model is initialized with a weak axisymmetric vortex located at the domain center (more details in Section 2.2). We use an f-plane assumption and do not prescribe any steering flow. The idealized TC can therefore stay nearly stationary as it evolves with time, making it possible to use static nests to cover the inner-core region.

A two-level nesting strategy is applied to gradually refine the grid spacing in the TC inner region (Figure S1 in Supporting Information S1). All computational grids are in the Cartesian coordinates. The coarsest parent grid, referred to as the Level 0 grid, is set at  $1,600 \times 1,600$  km wide with a 2 km uniform horizontal grid spacing. Such a domain is sufficiently large to encompass the entire TC. Periodic boundary conditions are applied at the east-west and south-north edges of the Level 0 grid. The Level 1 nested grid, with a 500 m grid spacing, is embedded in a  $400 \times 400$  km area centered around the central point of the Level 0 grid. Furthermore, the Level 2 nested grid, with a 125 m grid spacing, is embedded within the innermost  $100 \times 100$  km area of the Level 1 grid. During the model integration, the Level 1 and 2 nested grids use boundary condition information from their own parent domains, which are Level 0 and Level 1 grids, respectively.

We use one-way nesting, meaning we do not let the nested domain feedback onto its parent. Therefore, the solutions from the three grids in their overlapping areas are expected to be different. Using one-way nesting allows us to compare the resolved fine-scale features from the Level 1 and Level 2 grids, providing insights into the resolution-dependency of the feature of interest. The three grids use the same vertical layer setup, which has 50 levels (10 levels below 850 mb) and a top at 20 mb.

## 2.2. Experiment Setup

The three computation domains (Level 0, Level 1 and Level 2 grids) are initialized with the same balanced axisymmetric vortex (Reed & Jablonowski, 2012). The initial vortex has a maximum wind of 20 m/s at 125 km radius, and is located at the central points of the three grids. The environmental temperature and moisture are set to resemble an tropical sounding as in Jordan (1958). We use a constant Coriolis parameter evaluated at  $15^\circ\text{N}$ , a fixed uniform sea surface temperature (SST) of 302 K, and also a fixed uniform insolation of  $390 \text{ W/m}^2$ .

The simulation we did is a full physics run, with a set of physical parameterizations that is consistent with the nested domain of the T-SHiELD configuration (Gao et al., 2021, 2023). We use the GFDL single-moment five-category microphysics scheme (Zhou et al., 2019), a turbulent kinetic energy-based eddy diffusivity mass flux (TKE-EDMF) boundary layer scheme (Han & Bretherton, 2019), the Rapid Radiative Transfer Model for General Circulation Models radiation scheme (Iacono et al., 2008), and the ocean surface roughness length scheme used in 2017 version of Hurricane Weather Research and Forecasting model (Biswas et al., 2018). The scale-aware deep and shallow convection parameterizations (Han et al., 2017) are used in the Level 0 grid, but are turned off in the Level 1 and Level 2 nested grids.

It is worth noting that the Level 1 ( $dx = 500$  m) and Level 2 ( $dx = 125$  m) grids are within the turbulent gray zone, in which the turbulent eddies, except for those with relatively large spatial scale, cannot be explicitly resolved. For consistency, we use the same one-dimensional vertical turbulent scheme, that is, TKE-EDMF, to handle the vertical diffusion in all three grids. The asymptotic mixing length for the TKE-EDMF scheme is capped at 150 m to ensure the turbulent diffusion coefficient has reasonable values under the TC conditions. Our results demonstrate that we achieve satisfactory outcomes with such a choice in terms of resolving the TC-scale flow and the fine-scale features.

The timestep for physical parameterization is set to 45 s for all three grids. The remapping and acoustic time steps for FV3 (Harris et al., 2020) are reduced with the decreasing grid spacing (the remapping timesteps are 22.5 s, 7.5 s, 1.875 s, respectively; the acoustic timesteps are 3.75 s, 0.9375 s, 0.2344 s, respectively). The entire simulation integrates for 96 hr (with the three grids integrating concurrently), encompassing the entire period from which the TC evolves from a weak vortex to a mature storm. No nudging or relaxation is applied to any fields during the simulation. Three-dimensional outputs are saved every 3 hr for analysis. To our knowledge, this is the first published effort to use  $O(100 \text{ m})$  grid spacing to simulate the entire TC intensification period.

### 3. Simulated TC Evolution

The simulated TC in all the three grids undergoes a quick adjustment period, followed by a rapid intensification period, and eventually reaches a relatively steady state (except for the Level 0 grid). Figure S2 in Supporting Information S1 illustrates the simulated TC intensification process in the three grids. Overall, the TCs in the three grids show a classic intensification process, that is the TC intensifies as the core region contracts (i.e., Radius of Maximum Wind (RMW) gets smaller). The TCs from the Level 1 and Level 2 grids show a similar behavior: Both have faster intensification rates and smaller RMW than that in the Level 0 grid during the rapid intensification stage (Hours 48–78), followed by a slowly intensifying stage (beyond Hour 78). A detailed examination of the differences between the two higher resolution grids and the Level 0 grid is beyond the scope of the present study. However, the result here indicates that we obtained reasonable TC intensification processes in our O(100 m) grid spacing simulation.

Focusing on the instantaneous surface wind field (Figure S3 in Supporting Information S1), it is clear the use of high-resolution makes a difference: Higher resolution leads to finer scale wind structure and stronger wind gusts. It is worth noting, as illustrated by Figure S2d and S3 in Supporting Information S1, that the geometry of the TC-scale horizontal flow is very similar in the two nested grids throughout the simulation, even though the Level 2 grid does not feedback onto the Level 1 grid. This is a desirable result, as the similar TC-scale flow setting facilitates an understanding of the resolution-dependency of the small-scale feature we are interested in.

## 4. Characteristics of the Finger Clouds

### 4.1. Feature Identification

Here we identify the presence of the finger clouds in our simulation and describe their bulk characteristics. Both our Level 1 and Level 2 nested grids capture the finger clouds in the inner-edge of the eyewall. Figure 1 shows selected instantaneous vertical velocity and cloud water mixing ratio at 850 mb from the two nested grids. Noticeably, alternating updrafts and downdrafts exist along the inner-edge of the eyewall, which are roughly elongated in the TC radial direction. The cloud condensates roughly coincide with the updrafts.

Our simulated finger-like features closely resemble the features identified in radar observations collected from strong TCs (Aberson et al., 2006; Mashiko & Shimada, 2021). Figure 2 shows a comparison of the radar-observed reflectivity (Aberson et al., 2006) from Hurricane Isabel (2003) when it was at Category-5 status, and the composite radar reflectivity inferred from our Level 1 and 2 nested grid plotted in a similar manner. Finger-like features notably exist along the inner-edge of the eyewall (highlighted area in Figure 2a). Our simulated features, which are also located radially inside of the eyewall, have a similar appearance and spatial scale as the observed features. Similar to the observed features, our simulated features also propagate cyclonically around the TC center with the mean TC flow. The agreement here indicates our simulation offers a unique opportunity to understand these features.

The finger clouds emerge at about Hour 60 of the simulation in both the Level 1 and Level 2 nested grid, when the simulated hurricane has reached a significant strength and well-defined eye and eyewall. They then occur persistently throughout the simulation (see more snapshots in Figure S4 in Supporting Information S1). The occurrence of the finger clouds might be overestimated in our simulation as the TC maintained nearly axisymmetric structure due to the idealized settings. However, in reality, when the TC is nearly axisymmetric, the finger features can indeed occupy a significant portion of the eyewall inner edge (see Figure 13 of Mashiko & Shimada, 2021).

The simulated finger clouds are roughly 2–5 km wide (measured along the azimuthal direction) and limited below 4 km height. Our simulation indicates that they are resolvable at a grid spacing of 500 m and finer, but not in the 2 km grid spacing grid. Comparing the features in the two high resolution nested grids, the finger-like features in the Level 2 nested grid seem to have finer structure and are less frequent than their counterparts in the Level 1 nested grid. Such a difference is expected according to the energy cascade theory. Finer grid spacing enables the resolution of smaller-scale features, allowing larger-scale eddies to transfer kinetic energy into smaller-scale turbulent eddies. However, the spatial scale of the finger clouds is similar in both nests, indicating that their scales are being reasonably represented at both grid spacings.

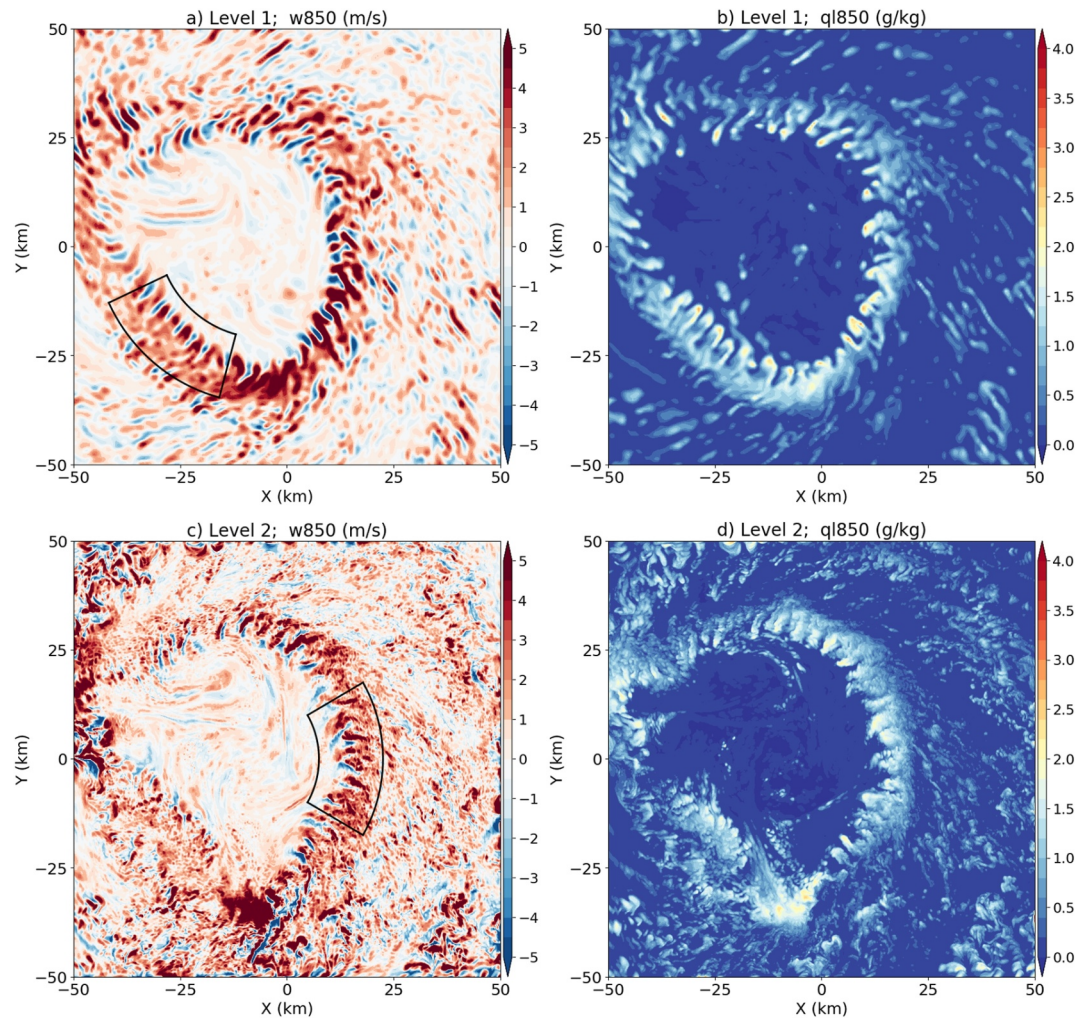


**Figure 1.** Instantaneous vertical velocity ( $w_{850}$ ) and cloud water mixing ratio ( $q_{l850}$ ) at 850 mb at Hour 66 from (a, b) Level 1 ( $dx = 500$  m) and (c, d) Level 2 ( $dx = 125$  m) nested grids. The outlined regions in panels (a, c) indicate the selected areas for later analysis.

#### 4.2. Feature Extraction

To better understand the three-dimensional structure and formation mechanism of the finger clouds, we apply a flow separation method that separates the TC-scale flow and the eddies responsible for the formation of the finger clouds. Considering the complicated geometry of the simulated TC-scale flow and the localized nature of the features of interest, we propose a regional mean and eddy separation method, with details described below.

- *Data extraction step.* We first identify areas in the TC-centered cylindrical coordinate that contain several eddy features of interest (Figures 1a and 1c). The TC center is defined as the location of the minimum surface pressure. Then we remap variables from these areas onto radial-azimuthal meshes (with constant increments in both radial and azimuthal directions); the horizontal winds are projected onto the TC-relative azimuthal and radial components.
- *Flow separation step.* We perform moving averaging along the azimuthal direction in the selected areas to obtain the mean flow. This choice recognizes that the TC-scale flow has strong variations along the radial direction but less along the azimuthal direction. The scope for the moving average is 6 degrees of azimuth. We iterate the averaging twice to ensure a clean mean-perturbation separation. The perturbation component is then obtained by subtracting the mean from the total field. Hereafter, we will refer to the mean and perturbation components obtained via this flow separation step as the TC-scale flow and eddy components, respectively.

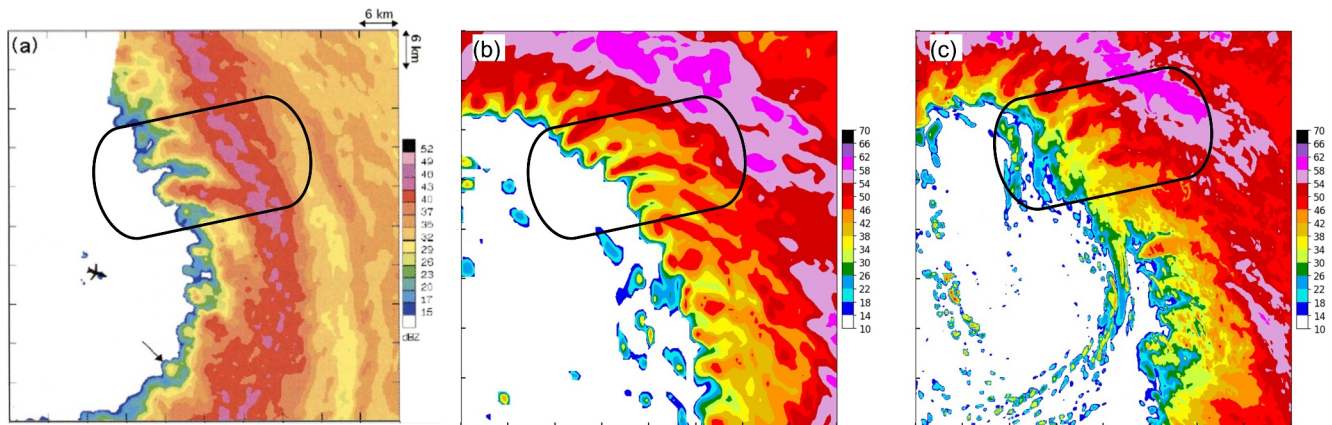


**Figure 2.** A comparison of the observed and model simulated radar reflectivity. (a) Radar reflectivity collected by aircraft from Hurricane Isabel (2003), adapted from Aberson et al. (2006), © American Meteorological Society. Used with permission. (b, c) model simulated composite radar reflectivity from the Level 1 and 2 nested grids, respectively. (b, c) are plotted in a manner as close as possible to (a). Note the model simulated radar reflectivity shown is the composite reflectivity, that is, the column-maximum reflectivity, which is different from the observed radar reflectivity in panel (a). The tick interval is the same in panels (a–c), which is 6 km in  $x$  and  $y$  directions. The selected areas highlight representative finger-like features.

Figure S6 in Supporting Information S1 demonstrates the results from applying the above flow separation method on the total tangential wind in the selected areas in Figures 1a and 1c. The resulting TC-scale flow component contains no visually noticeable fine-scale perturbations and also retains its natural radial variation. The eddy component contains no noticeable residual TC-scale flow. We apply the same method to all variables at all levels to get the three-dimensional data for the eddies and TC-scale flow in the selected areas.

### 4.3. Eddy Structure

Here we examine the structure of the eddies responsible for the formation of the finger clouds. Figure 3 illustrates typical eddy vertical velocity fields in Level 1 and 2 nested grids. Although the eddy features in the Level 2 grid are more detailed and stronger than those in the Level 1 grid, the eddies in the two nested grids exhibit many similar characteristics, which are summarized below.

- They are characterized by a classic horizontal roll vortices structure, roughly elongated along the TC radial direction, which is the main reason for finger-like appearance of the clouds they cause.
- They feature overturning circulations along the vertical-azimuthal plane, with their azimuthal and vertical velocity components constituting their overturning circulations.
- Their vertical wind components are tilted against the TC tangential wind in the lower levels (approximately below 1 km), a signature of shear-driven eddies (more details in Section 5).
- They are mostly located within the RMW (determined by the azimuthal-average surface wind speed in the selected area), and have a radial extent of about 10 km.
- Their updrafts and downdrafts peak at 1–2 km heights and are roughly confined below 4 km. The peak eddy vertical velocity shifts upward with increasing radius. Increased and decreased cloud condensates roughly overlap with the updraft and downdraft cores, respectively (not shown).
- Their azimuthal wavelength, defined as the distance between nearby updrafts along the azimuthal direction, is roughly 2–4 km.
- Their updraft magnitude is on the order of 5 m/s and can reach up to 10 m/s in the 125 m grid spacing grid.

### 5. Formation Mechanism

Here we examine the eddy kinetic energy (EKE) budget to identify the dominant EKE production terms, which could shed insight on their formation mechanism. Since these features are localized and formed in a highly sheared environment, we hypothesize that they are formed via a type of shear instability. Following the EKE budget equation in Nolan (2012), the shear production terms can be written as:

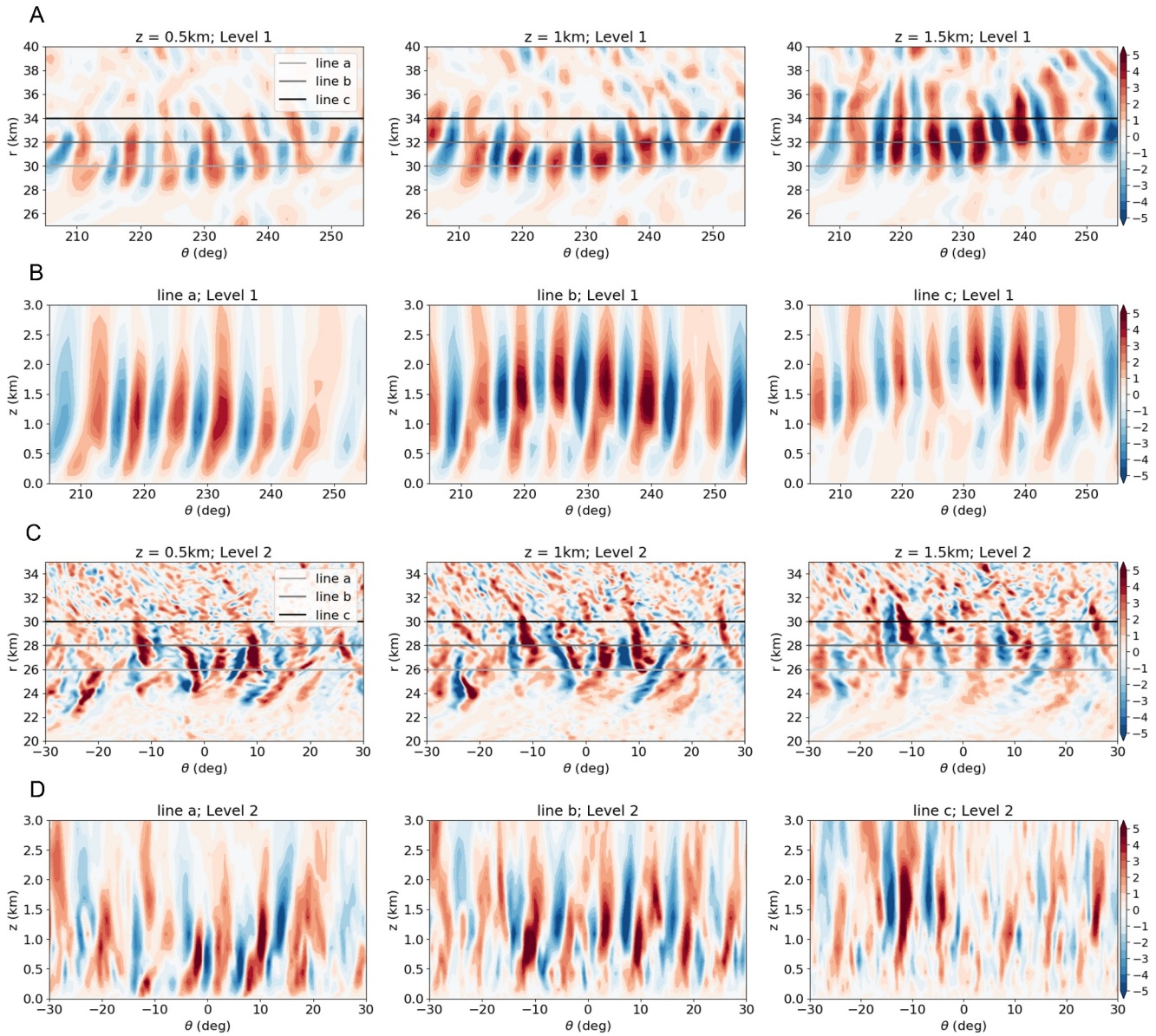


**Figure 3.** Instantaneous eddy vertical velocity ( $w'$ ; m/s) from Level 1 and Level 2 nested grids. Row A shows  $w'$  on the  $r$ - $\theta$  plane at three levels from the Level 1 nested grid (Figure 1a). Row B shows cross-sections of  $w'$  along three selected arcs (indicated by the three lines in Row A). Row C shows  $w'$  on the  $r$ - $\theta$  plane at three levels from the Level 2 nested grid (Figure 1c). Row D shows cross-sections of  $w'$  along three selected arcs (indicated by the three lines in Row C). The darkest black lines (line c) in Rows A and C corresponds to the Radius of Maximum Wind at the surface.

$$\begin{aligned} \frac{\partial E'}{\partial t} = & - \left[ \overline{u'v'} \left( \frac{\partial \bar{v}}{\partial r} - \frac{\bar{v}}{r} \right) \right]_{V\_R} - \left[ \overline{u'u'} \frac{\partial \bar{u}}{\partial r} + \overline{v'v'} \frac{\bar{u}}{r} \right]_{U\_R} \\ & - \left[ \overline{u'w'} \frac{\partial \bar{w}}{\partial r} \right]_{W\_R} - \left[ \overline{v'w'} \frac{\partial \bar{v}}{\partial z} \right]_{V\_Z} - \left[ \overline{u'w'} \frac{\partial \bar{u}}{\partial z} \right]_{U\_Z} - \left[ \overline{w'w'} \frac{\partial \bar{w}}{\partial z} \right]_{W\_Z} + \dots \end{aligned}$$

where  $u$ ,  $v$ ,  $w$  are the three wind components in the azimuthal, radial and vertical directions, respectively. The overbar and prime signs denote the TC-scale and eddy flow components, respectively.  $E'$  is the EKE and defined as  $0.5*(u'^2+v'^2+w'^2)$ . The  $V\_R$ ,  $U\_R$ ,  $W\_R$  ( $V\_Z$ ,  $U\_Z$ ,  $W\_Z$ ) terms in the above equation denote the EKE production by the radial (vertical) shear of the tangential, radial and vertical TC-scale wind components, respectively. Here we do not intend to examine all terms in the EKE budget equation because of the challenges in

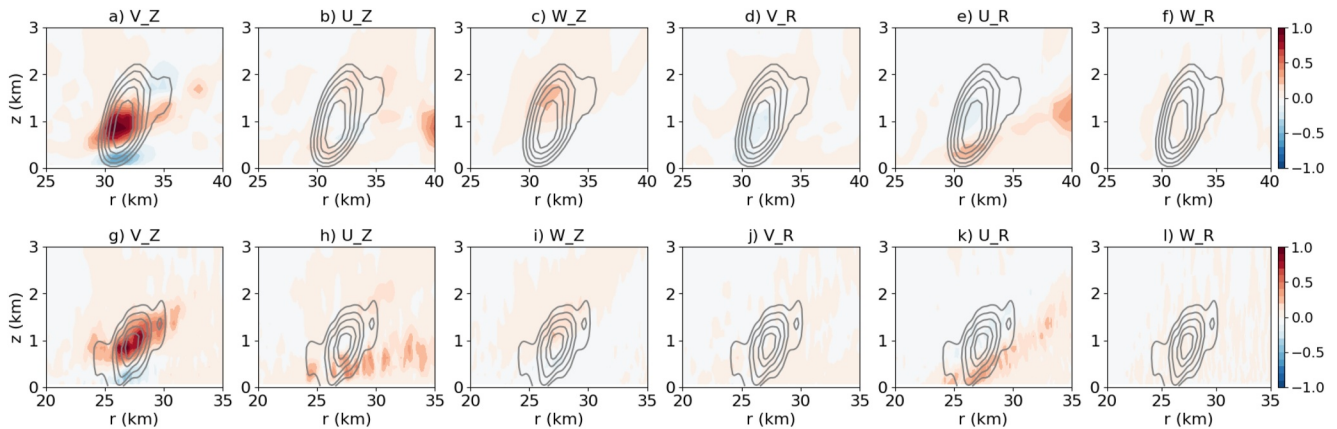


**Figure 4.** Azimuthal-averaged shear production terms in the eddy kinetic energy (EKE) budget equation. Their values are normalized by the maximum value of the  $V_Z$  term (the production due to the vertical shear of the tangential wind). Upper row: for eddies in the Level 1 nested grid (selected region in Figure 1a). The contour lines show the normalized azimuthal-averaged EKE (normalized by its maximum value; contour interval is 0.15). Lower row: Same as the upper row, but for the eddies in the Level 2 nested grid (selected region in Figure 1c).

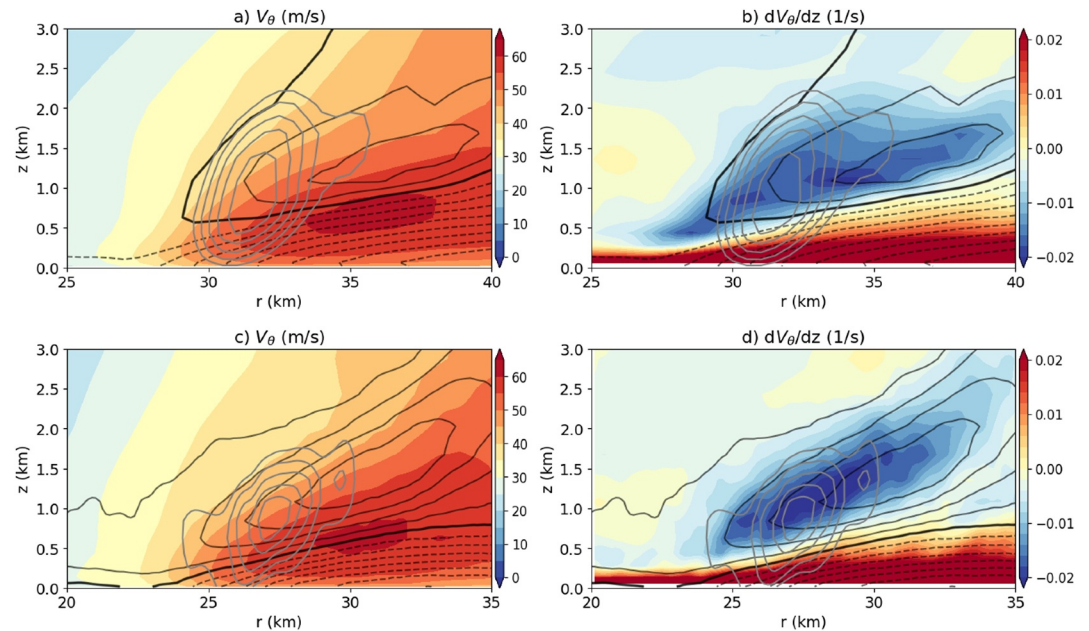
diagnosing the time tendency term (which requires high frequency outputs) and the dissipation term (which requires the dissipation coefficients that were not saved). We anticipate that shear production is the only positive contributor to EKE tendency, while buoyancy work (Figure S5 in Supporting Information S1) and dissipation exert negative influences. Our following analysis therefore focuses on identifying the dominant shear component contributing to EKE tendency.

Figure 4 shows the azimuthal-averaged shear production terms, which are for the eddies shown in Figure 3. For both eddy cases, the  $V_Z$  term (i.e., the shear production due to the vertical shear of the tangential wind) is the predominant term, and this term has the largest value at the region where the EKE reaches its peak value. This is true for all the eddy cases we have examined from both nested grids. The EKE budget analysis therefore indicates that the eddies are primarily driven by the shear instability associated with the vertical distribution of the tangential wind in the TC inner region.

The question arises whether a strong shear layer exists that can provide a conducive environment for the eddy formation and how such a shear layer is maintained. Figure 5 shows the distribution of the azimuthal-averaged TC tangential wind and its vertical shear in the two selected cases (Figures 1a and 1c), overlaid with the azimuthal-averaged EKE and TC radial wind for interpretation. The region with the strongest EKE indeed overlaps with a strong negative vertical tangential wind shear layer. The  $V_Z$  production term in the EKE budget equation is always positive in this shear layer, making a positive contribution to the growth of EKE. Interestingly, this negative vertical tangential wind shear layer overlaps with the radial outflow that exists above the BL inflow layer in the TC inner-core region. This radial outflow layer exists because of the radially outward acceleration associated with the super-gradient tangential flow in the TC inner region (Montgomery & Smith, 2017), which is expected to be a common feature among TCs, especially for simulated TCs in idealized settings. The negative tangential wind shear layer is formed due to the radial outflow: The radial outflow leads to the deceleration of the tangential wind because of the conservation of absolute angular momentum, which thus causes the vertically decreasing tangential wind in the TC inner region (within RMW; Figure 5).

Our analysis therefore has established a linkage between the TC-scale dynamics and the eddy features responsible for the formation of the finger clouds. We propose that the negative vertical tangential wind shear layer, caused by the low-level radial outflow in the TC inner region, can lead to the formation of the eddy features due to a Kelvin-Helmholtz type of instability once the shear becomes strong enough to overcome the stable stratification. Our proposed mechanism answers the following questions regarding the key characteristics of the eddy features and the finger cloud they caused.

1. *Why do the finger clouds emerge when the simulated TC becomes sufficiently strong?* This may be because the magnitude of the vertical tangential wind shear responsible for the eddy formation is directly related to the TC



**Figure 5.** Upper row: Azimuthal-averaged Tropical Cyclone (TC) tangential wind (a) and its vertical shear (b) based on the data from the Level 1 nested grid (selected region in Figure 1a); the gray contours show the normalized azimuthal-averaged eddy kinetic energy (contour interval is 0.15); the black contours show the azimuthal-averaged TC radial wind (thick line indicates 0 value; contour interval is 2.5 m/s). Lower row: Same as the upper row but based on the data in the Level 2 nested grid (selected region in Figure 1c). The Radius of Maximum Wind at the surface is 34 and 30 km for the TCs in Level 1 and Level 2 nested grids, respectively.

- intensity. The TC needs to be strong enough to develop the vertical tangential wind shear necessary to overcome buoyancy suppression.
2. *Why do the finger clouds in the idealized simulation occur frequently after their emergence?* The TC-scale flow features (the radial outflow and the associated negative vertical tangential wind shear layer) responsible for the eddy formation are expected to be common features for mature TCs. Therefore, the conducive environment for the eddy formation persists, leading to the frequent occurrence of finger clouds.
  3. *Why are the finger clouds located radially inside of the RMW?* This is because the negative vertical tangential wind shear layer mostly lies radially inside of the RMW.
  4. *Why are the eddies vertically confined and featured with an upward shift with increasing radius?* This might be due to vertical extent and the vertical-radial geometry of the negative vertical tangential wind shear layer. Additionally, the radial slope of TC eyewall updraft could also contribute to the upward shift of the eddy features with radius.

## 6. Summary and Discussion

This study presents a  $O(100\text{ m})$  grid spacing simulation that covers the entire core region of an idealized TC, which successfully captured the finger-like clouds located along the inner-edge of the TC eyewall, resembling the observed features. We documented the key characteristics of the eddy features responsible for the formation of these finger clouds and proposed that these features are formed primarily due to the shear instability associated with the tangential wind distribution in the TC inner region. Our proposed mechanism explains several key characteristics of these features, including their emergence time, frequency, relative radial location, and radial-vertical geometry.

We acknowledge here that previous studies have speculated that the finger-like features are formed by Kelvin-Helmholtz type instability (or the shear instability; Aberson et al., 2006; Tsukada & Horinouchi, 2020). But no physical or quantitative analysis has been done yet. Ito et al. (2017) suggested that the roll-like features (referred to as Type-3 rolls) in the TC inner region might be due to a parallel instability, although no direct analysis is offered to support this argument. One important contribution of this study is that we leveraged our

three-dimensional high-resolution model simulation data to identify the key flow component that is responsible for the formation of these features. We believe these finger-like features become resolvable at 500 m grid spacing, and should be common features at  $O(100\text{ m})$  grid spacing simulations. Our analysis provides a reference for interpreting these fine-scale features in existing and future modeling studies.

As indicated by previous studies (e.g., Mashiko & Shimada, 2021; Tsukada & Horinouchi, 2020), the existence of the eddy features in the TC inner region carries several implications. First, we notice they are able to transport the high-momentum air down to the surface, and cause extreme wind gusts within the TC inner region. Figure S7 in Supporting Information S1 illustrates that they cause localized regions with enhanced wind, with instantaneous surface wind speeds significantly greater than those at RMW (i.e., the radius for the maximum surface azimuthal-averaged wind), particularly in the 125 m grid spacing nested grid. Second, these features are associated with periodic regions with enhanced diabatic heating located below 3 km height and inside of the RMW (Figure S8 in Supporting Information S1), which may have an impact on the intensification of the entire TC vortex. The response of the entire TC vortex to such heating warrants future investigation.

The simulation we presented is not a Large Eddy Simulation (LES) yet, as the finest grid spacing is limited to 125 m. We cannot fully resolve the sub-kilometer vortices in the TC inner-core region, which are reported to cause more extreme low-level updrafts and winds (Stern et al., 2016). Nevertheless, we showcased the possibility of using multi-level nesting to achieve  $O(100\text{ m})$  horizontal grid spacing for real world TC simulation and prediction, which is a direction for the next generation of TC models. This study also presents an initial effort toward GFDL's strategy for achieving  $O(100\text{ m})$  and even finer grid spacing for TC simulation. The flexible horizontal and vertical nesting capacity in FV3 enables the model to achieve  $O(10\text{ m})$  grid spacing both horizontally and vertically in the TC core region. Our future development work will focus on implementing a TKE-based three-dimensional subgrid closure scheme into FV3, which will further enhance its application to the turbulence-resolving regime.

## Data Availability Statement

The model simulation data used for the analysis of this paper can be found at Gao (2024).

## References

- Aberson, S. D., Montgomery, M. T., Bell, M., & Black, M. (2006). Hurricane Isabel (2003): New insights into the physics of intense storms. Part II: Extreme localized wind. *Bulletin American Meteorology Social*, 87, 1349–1354. <https://doi.org/10.1175/BAMS-87-10-1349>
- Biswas, M. K., Bernardet, L., Abarca, S., et al. (2018). Hurricane Weather Research and Forecasting (HWRF) Model: 2017 Scientific Documentation. <https://doi.org/10.5065/D6MK6BPR>
- Gao, K. (2024). Finger clouds simulated by two-level nested SHIELD [Dataset]. *Zenodo*. <https://doi.org/10.5281/zenodo.11553088>
- Gao, K., Harris, L., Zhou, L., Bender, M., Chen, J. H., Zhou, L. J., & Knutson, T. (2023). Regulating fine-scale resolved convection in high-resolution models for better hurricane track prediction. *Geophysical Research Letters*, 50(13), e2023GL103329. <https://doi.org/10.1029/2023gl103329>
- Gao, K., Harris, L., Zhou, L., Bender, M. A., & Morin, M. J. (2021). On the sensitivity of hurricane intensity and structure to horizontal tracer advection schemes in FV3. *Journal of the Atmospheric Sciences*, 78(9), 3007–3021. <https://doi.org/10.1175/JAS-D-20-0331.1>
- Han, J., & Bretherton, C. S. (2019). TKE-based moist eddy-diffusivity mass-flux (EDMF) parameterization for vertical turbulent mixing. *Weather and Forecasting*, 34(4), 869–886. <https://doi.org/10.1175/WAF-D-18-0146.1>
- Han, J., Wang, W., Kwon, Y. C., Hong, S., Tallapragada, V., & Yang, F. (2017). Updates in the NCEP GFS cumulus convection schemes with scale and aerosol awareness. *Weather and Forecasting*, 32(5), 2005–2017. <https://doi.org/10.1175/WAF-D-17-0046.1>
- Harris, L., Zhou, L., Lin, S., Chen, J., Chen, X., Gao, K., et al. (2020). GFDL SHIELD: A unified system for weather-to-seasonal prediction. *Journal of Advances in Modeling Earth Systems*, 12(10), e2020MS002223. <https://doi.org/10.1029/2020ms002223>
- Iacono, M. J., Delamere, J. S., Mlawer, E. J., Shephard, M. W., Clough, S. A., & Collins, W. D. (2008). Radiative forcing by long-lived greenhouse gases: Calculations with the AER radiative transfer models. *Journal of Geophysical Research*, 113(D13), D13103. <https://doi.org/10.1029/2008JD009944>
- Ito, J., Oizumi, T., & Niino, H. (2017). Near-surface coherent structures explored by large eddy simulation of entire tropical cyclones. *Scientific Reports*, 7(1), 3798. <https://doi.org/10.1038/s41598-017-03848-w>
- Jordan, C. L. (1958). Mean soundings for the west indies area. *Journal of the Atmospheric Sciences*, 15(1), 91–97. <https://doi.org/10.1175/1520-0469>
- Kossin, J. P., & Schubert, W. (2004). Mesovortices in hurricane Isabel. *Bulletin American Meteorology Social*, 85(2), 151–153. <https://doi.org/10.1175/BAMS-85-2-151>
- Mashiko, W., & Shimada, U. (2021). Observed near-surface wind structure in the inner core of typhoon goni (2015). *Monthly Weather Review*. <https://doi.org/10.1175/mwr-d-20-0294.1>
- Montgomery, M. T., & Smith, R. K. (2017). Recent developments in the Fluid dynamics of tropical cyclones. *Annual Review of Fluid Mechanics*, 49(1), 1541–1574. <https://doi.org/10.1146/annurev-fluid-010816-060022>
- Mouallef, J., Harris, L., & Benson, R. (2022). Multiple same-level and telescoping nesting in GFDL's dynamical core. *Geoscientific Model Development*, 15(11), 4355–4371. <https://doi.org/10.5194/gmd-15-4355-2022>

## Acknowledgments

The authors would like to thank Tim Marchok for discussions during the preparation of this manuscript, and the two reviewers who provided constructive comments in the review process. This research was funded by award NA23OAR4320198 from the National Oceanic and Atmospheric Administration, U.S. Department of Commerce. This work was substantively supported by the NOAA Research Global-Nest Initiative. The statements, findings, conclusions, and recommendations are those of the authors and do not necessarily reflect the views of the National Oceanic and Atmospheric Administration, or the U.S. Department of Commerce.

- Nolan, D. S. (2012). Three-dimensional instabilities in tornado-like vortices with secondary circulations. *Journal of Fluid Mechanics*, 711, 61–100. <https://doi.org/10.1017/jfm.2012.369>
- Reed, K. A., & Jablonowski, C. (2012). Idealized tropical cyclone simulations of intermediate complexity: A test case for AGCMs. *Journal of Advances in Modeling Earth Systems*, 4(2). <https://doi.org/10.1029/2011ms000099>
- Rotunno, R., Chen, Y., Wang, W., Davis, C., Dudhia, J., & Holland, G. J. (2009). Large-eddy simulation of an idealized tropical cyclone. *Bulletin of the American Meteorological Society*, 90(12), 1783–1788. <https://doi.org/10.1175/2009bams2884.1>
- Stern, D. P., George, B. H., & Aberson, S. D. (2016). Extreme low-level updrafts and wind speeds measured by dropsondes in tropical cyclones. *Monthly Weather Review*, 144(6), 2177–2204. <https://doi.org/10.1175/MWR-D-15-0313.1>
- Tsukada, T., & Horinouchi, T. (2020). Estimation of the tangential winds and asymmetric structures in typhoon inner core region using Himawari-8. *Geophysical Research Letters*, 47(11), e2020GL087637. <https://doi.org/10.1029/2020GL087637>
- Zhou, L., Lin, S.-J., Chen, J.-H., Harris, L. M., Chen, X., & Rees, S. L. (2019). Toward convective-scale prediction within the next generation global prediction system. *Bulletin of the American Meteorological Society*, 100(7), 1225–1243. <https://doi.org/10.1175/BAMS-D-17-0246.1>